JGR Planets

RESEARCH ARTICLE
10.1029/2019JE006176

Key Points:
- New X-Ray diffraction measurements covering the entire range of ice II, III, V and VI using state of the art high pressure techniques
- The first Gibbs energy equations of states for ice II, III, V and VI (and first equations of state for ice II, III and V)
- New open-source code SeaFreeze allows to explore water and ices thermodynamic at all conditions found in solar system planetary hydrospheres

Supporting Information:
- Supporting Information S1

Correspondence to:
B. Journaux,
baptiste.journaux@gmail.com

Citation:
Journaux, B., Brown, J. M., Pakhomova, A., Collings, I. E., Petitgirard, S., Espinoza, P., et al. (2020). Holistic approach for studying planetary hydrospheres: Gibbs representation of ices thermodynamics, elasticity, and the water phase diagram to 2,300 MPa. *Journal of Geophysical Research: Planets*, *125*, e2019JE006176. https://doi.org/10.1029/2019JE006176

Received 19 AUG 2019
Accepted 7 DEC 2019
Accepted article online 17 DEC 2019

Author Contributions:
Conceptualization: B. Journaux, J. M. Brown
Data curation: B. Journaux, J. M. Brown, A. Pakhomova, I. E. Collings, T. Boffa Ballaran
Formal analysis: B. Journaux, J. M. Brown, A. Pakhomova, I. E. Collings, T. Boffa Ballaran
Funding acquisition: B. Journaux, J. M. Brown
Investigation: B. Journaux, A. Pakhomova, I. E. Collings, S. Petitgirard, S. D. Vance
Methodology: B. Journaux, J. M. Brown
Project administration: B. Journaux, J. M. Brown
(continued)

©2019. American Geophysical Union. All Rights Reserved.

Holistic Approach for Studying Planetary Hydrospheres: Gibbs Representation of Ices Thermodynamics, Elasticity, and the Water Phase Diagram to 2,300 MPa

B. Journaux[1], J. M. Brown[1], A. Pakhomova[2], I. E. Collings[3,4], S. Petitgirard[5], P. Espinoza[1], T. Boffa Ballaran[6], S. D. Vance[7], J. Ott[1,8], F. Cova[3,9], G. Garbarino[3], and M. Hanfland[3]

[1]Department of Earth and Space Sciences, University of Washington, Seattle, WA, USA, [2]Photon Sciences, Deutsches Elektronen-Synchrotron, Hamburg, Germany, [3]European Synchrotron Radiation Facility, Grenoble, France, [4]Center for X-ray Analytics, Empa-Swiss Federal Laboratories for Materials Science and Technology, Zürich, Switzerland, [5]Institute für Geochemie und Petrologie, ETH Zurich, Zürich, Switzerland, [6]Bayerisches Geoinstitut, Univesitaet Bayreuth, Bayreuth, Germany, [7]Jet Propulsion Laboratory, California Institute of Technology, Pasadena, CA, USA, [8]Department of Earth and Planetary Sciences, University of California Santa Cruz, Santa Cruz, CA, USA, [9]Department of Physic, Norwegian University of Science and Technology, Trondheim, Norway

Abstract Gibbs energy representations for ices II, III, V, and VI are reported. These were constructed using new measurements of volumes at high pressure over a range of low temperatures combined with calculated vibrational energies grounded in statistical physics. The collection of representations are released within the open source SeaFreeze program, together with the Gibbs representation already known for ice Ih and water. This program allows accurate determination of thermodynamics properties (phase boundaries, density, specific heat, bulk modulus, thermal expansivity, chemical potentials) and seismic wave velocities over the entire range of conditions encountered in hydrospheres in our solar system (130–500 K to 2,300 MPa). These comprehensive representations allow exploration of the rich spectrum of thermodynamic behavior in the H_2O system. Although these results are broadly applicable in science and engineering, their use is particularly relevant to habitability analysis, interior modeling, and future geophysical sounding of water-rich planetary bodies of our solar system and beyond.

1. Introduction

Water is a fundamentally important molecule in scientific fields ranging from biology to engineering, earth and environmental sciences, chemistry, or astrophysics. As a common molecular species in our cosmic neighborhood (Hanslmeier, 2011), water ice polymorphs at high pressures in planetary interiors could be the most abundant "mineral group" in the Universe. A focus on potentially habitable hydrospheres of icy moons, small bodies such as Pluto and Ceres, and ocean exoplanets (Sotin & Tobie, 2004; S. Vance & Brown, 2013; B Journaux et al., 2013; Baptiste Journaux et al., 2017; Noack et al., 2016; Kite & Ford, 2018; Unterborn et al., 2018; Hendrix et al., 2019) motivates an interest in thermodynamic properties of water and ices in the <200 MPa range. For example, the presence of an insulating layer of high-pressure ice between the deep ocean and the underlying silicates on large water-rich planetary bodies has been identified as a potential bottleneck for habitability, as it could limit nutrient transport (Léger et al., 2004; Noack et al., 2016; Baptiste Journaux et al., 2017; Kite & Ford, 2018). Thus, accurate thermodynamic representations for all stable phases of water and aqueous solutions are essential in the analysis of potential planetary habitability.

Unfortunately, sparse measurements at high pressure, some performed more than 100 years ago, limit our understanding of high-pressure ice thermodynamics and phase equilibria (Salzmann, 2018). In order to better constrain the structure, evolution, and habitability of the interiors of water-rich planetary bodies, a new generation of accurate measurements and internally consistent thermodynamic representations of aqueous solutions and ice polymorphs is required. Furthermore, since next-generation planetary exploration missions are likely to investigate the seismic structure of icy worlds (Vance, Kedar, et al., 2018; Vance, Panning, et al., 2018; Panning et al., 2018; R. D. Lorenz et al., 2019; Stähler et al., 2019), data on seismic wave speeds in ices and aqueous solutions as a function of pressure and temperature are also needed.

Resources: B. Journaux, A. Pakhomova, I. E. Collings, S. Petitgirard, T. Boffa Ballaran, J. Ott, F. Cova, G. Garbarino, M. Hanfland
Software: B. Journaux, J. M. Brown, P. Espinoza
Supervision: B. Journaux, J. M. Brown
Validation: B. Journaux, J. M. Brown
Visualization: B. Journaux
Writing - original draft: B. Journaux
Writing – review & editing: B. Journaux, J. M. Brown

Bridgman (1912) provided the first delimitation of the phase boundaries for ices Ih, II, III, V, and VI. These measurements and additional work for the phase boundary of ices VI–VII (Bridgman, 1937) constitute the main—and sometimes only—constraints for the water phase diagram boundaries below 2,000 MPa (M Choukroun & Grasset, 2007; Dunaeva et al., 2010; Tchijov, 2004; Wagner et al., 2011). Bridgman provided numerous pressure-temperature points along the phase boundaries as well as volume changes measured using the displacement of the piston of his high-pressure apparatus. Crystal structures and absolute volume measurements of ice polymorphs came later as X-ray and neutron diffraction measurements were obtained on metastable (quenched) samples retrieved cryogenically (B. Kamb et al., 1967; Barclay Kamb, 1965; Barclay Kamb & Davis, 1964; McFarlan, 1936a, 1936b). Surprisingly, few additional measurements have been reported for these ices since the pioneering work of the previous century.

Current thermodynamic representations for water and ices at high pressure (Choukroun & Grasset, 2007; Choukroun & Grasset, 2010; Dunaeva et al., 2010; Tchijov, 2004) use ad hoc parameterizations to independently compute chemical potentials, volumes, and specific heats. Since all equilibrium thermodynamic quantities (e.g., volume, chemical potential, bulk modulus, thermal expansivity) are derived from an underlying thermodynamic potential (e.g., Gibbs energy), properties should not be independently parameterized. While prior models were adjusted to reproduce observed phase equilibria and volume changes by Bridgman (1912), they remain thermodynamically inconsistent (cross derivatives do not match), which precludes accurate determination of other thermodynamic properties. As one example, the specific heats for ice polymorphs given by Tchijov (2004) and used in the current planetary dynamic models are significantly overestimated by up to 35%. This leads to an underestimate of temperature gradients within convective layers. Extrapolations of properties beyond the range of experimental constraints are not reliable, and the substantial effort necessary to implement these representations remains a barrier to their widespread use.

Full Gibbs energy representations are available for a small number of materials. The conventional approach, articulated by Span (2000) and used to create a representation for ice Ih (Feistel & Wagner, 2006), has proven to be tedious. Custom and hard-to-implement equations are required for each material, moreover modification in the face of new measurements has proven essentially impossible. An alternative approach, described in Brown (2018), uses "local" basis function (LBF) representations in the form of tensor b-splines. The advantages of such representations include (i) the ease in creating or modifying the representation for an energy potential (e.g., Gibbs energy), (ii) the "universal" form of the parameterization (requiring no custom coding for individual materials), (iii) an ability to reproduce complex local surface features without impacting the global quality of the fit, and (iv) the straightforward computation of thermodynamic properties through calculations based on analytic derivatives. Recent work on liquid water to 2,300 MPa over a range of temperatures demonstrates the utility of the approach in representing water's complex behavior (Bollengier et al., 2019). The main obstacle to the extension of that effort to high-pressure ice polymorphs III, V, and VI has been the lack of adequate in situ high-pressure measurements that extend below room temperature.

The compressibility and thermal properties of D_2O ice II have been investigated experimentally by Lobban et al. (2002) and Fortes et al. (2005). Earlier work was likely affected by systematic errors as the ice II structure was probably contaminated with helium (see discussion in Lobban et al., 2002; Fortes et al., 2005). Gagnon et al. (1990) gave an isothermal (238 K) equation fitted to four unreported data points.

Volume measurements at high pressure using neutron diffraction with D_2O ice III were reported by Londono et al. (1998) (3 data points at 245–250 K) and Lobban et al. (2000) (5 data points in the 250–330 MPa and 240–250 K range). Two piston-displacement points for ice III at 248 K are given by Shaw (1986). The Gagnon et al. (1990) isothermal equation provides unrealistic volumes, as pointed out by Choukroun and Grasset (2007).

Two piston-displacement points (248 K) from Shaw (1986) and a density-pressure law from Gagnon et al. (1990) are reported for ice V. The latter again provides unreasonable volumes, as also noted above for ice III. D_2O ice V neutron diffraction volumes were collected over a wider range, and represent to this day the largest data set for ice V, with 11 points in the 400–500 MPa and 100–254 K range (Colin Lobban et al., 2000).

The first extensive pressure-temperature-volume data for H_2O ice VI were published by Bezacier et al. (2014), but only above 300 K. A review of other data sets for H_2O and D_2O ice VI measurements is also provided in Bezacier et al. (2014).

To provide the requisite data for constructing better thermodynamic representations, we obtained new X-ray diffraction measurements for ices II, III, V, and VI in a pressure regime from 200 to 2,000 MPa for temperatures between 180 and 270 K. Mie-Grüneisen equations of states were determined, where pressure is separated into the cold (zero Kelvin) compression plus a thermal pressure calculated using quasi-harmonic vibrational energies based on phonon densities of states constrained by measurements and theory. The resulting representation of Gibbs energy for each of the ices and for liquid water (Bollengier et al., 2019), using the framework described in Brown (2018), then provides a fundamental and robust description of their thermodynamic properties. Phase equilibria (solid-solid and solid-liquid) are determined as the locus of pressure-temperature points with equal chemical potential. Equilibrium thermodynamic properties (e.g., density, specific heat, bulk modulus, thermal expansivity, entropy, and enthalpy) are derived from appropriate analytic derivatives of Gibbs energy. In addition, isotropic seismic wave velocities are estimated for all polymorphs as a function of pressure and temperature using a volume and temperature dependent shear modulus that is constrained by the ultrasonic and Brillouin measurements at high pressure, combined with the adiabatic bulk modulus from the Gibbs energy representation.

This toolkit for predicting thermodynamic properties of water and ices, referred to as SeaFreeze, has been released as open source code. It allows a self-consistent exploration of thermodynamic properties and elasticity of water and ices over a large range of pressure-temperature conditions, applicable to all planetary hydrospheres occurring in our solar system. Very high pressure body-centered cubic ice VII and ice X ices, expected in thick hydrospheres of ocean exoplanets, will be implemented in SeaFreeze in the near future. Their much larger stability fields, second order phase transitions and complex proton dynamics (Hernandez & Caracas, 2016, 2018), necessitate a dedicated study to obtain a satisfying representation, which is beyond the scope of the present work. An anticipated extension of SeaFreeze will also include solute thermodynamics.

2. Methods

2.1. Volume Determinations at High Pressure

Ultrapure MiliQ™ water was loaded in a diamond anvil cell with 500 to 600 μm culets diamonds and indented 80 μm thick stainless-steel gaskets, with a 300 μm in diameter pressure chamber. Ruby was used as a pressure calibrant, with a precision of 30 MPa, using an external reference ruby in contact with the back of the anvil to correct for the temperature dependence of the fluorescence. Temperature was regulated using a He-cryostat. X-ray diffraction data were collected at the ID15B beamline of the European Synchrotron Radiation Facility, Grenoble, France, using a wavelength of 0.41137 Å and a beam diameter of 10 × 10 μm. Diffraction images were collected using a MAR555 flat panel detector. The detector-to-sample distance was calibrated with a silicon standard using the procedure implemented in Fit2D. The program Dioptas (Prescher & Prakapenka, 2015) was used for masking diamond peaks and integrating the 2-D images into 1-D powder diffraction patterns. Powder diffraction data were collected by a continuous ω rotation of ±5°, with a 2 s exposure time. In the case of single crystals, a continuous ω rotation of ±20° with 2 s exposures was used. LeBail refinements of the powder diffraction patterns were performed using Topas (Coelho, 2018). All diffraction patterns measured exhibited texturing, and thus Pawley refinements were used to determine the unit cell variation at different temperature and pressure conditions.

Powder of ice II was obtained by cooling liquid water at 390 MPa down to 180 K by 1 K/min. Strain could be observed in some of diffraction patterns which presented very broad features at pressure >450 MPa. These were removed from the present data sets.

Ice III was formed by cooling water to 220 K at 300 MPa. It was metastable in this range as these conditions correspond to the stability field of ice II. Diffraction measurements taken directly after freezing at 220 K showed texturing and strain upon formation, with no clear volume-pressure dependence, and were therefore not considered. Upon heating, relaxation was observed, along with the formation of larger crystal domains, and a clear volume trend with temperature could be measured. Both single crystal data (step scans ±25° every 0.5°) and single frame images (continuous ±20° rotation scan) were measured and integrated with CrysAlisPro or Dioptas, respectively. Both refinements were included in the fit of the equation of state.

Ice V was crystallized in its stability field by cooling liquid water at 560 MPa to 230 K. Upon heating and decompression, at ~450 MPa and 245 K the appearance of single reflections of an unknown phase was

Table 1
Relationship of Thermodynamic Quantities to Derivatives of Gibbs Energy

Thermodynamic quantity	Symbol	Derivatives w.r.t G
Specific volume	V	G_p
Entropy	S	$-G_T$
Specific heat (constant pressure)	C_p	$-T\,G_{2T}$
Isothermal bulk modulus	K_t	$-G_p\,G_{2p}^{-1}$
Adiabatic bulk modulus	K_s	$\frac{G_p G_{2T}}{G_{pT}^2 - G_{2T} G_{2p}}$
Thermal expansivity	α	$G_{pT}\,G_p^{-1}$

Note. Subscripts on G denote the appropriate partial derivative with p for pressure, T for temperature.

observed. The new phase could not be identified with known water polymorph structures and will be the subject of future studies. Ice V and the new phase coexisted over the range of ~220–260 K and 450–550 MPa. Upon heating, the ice V underwent progressive texturing, indicated by substitution of the powder-like rings by sharp diffraction peaks. Several pressure-temperature points were excluded from the fit due to the texturing of ice V and/or dominated presence of the unknown phase.

Polycrystalline ice VI was obtained by compressing ice V above 650 MPa at 220 K. As for ice III, data collected at 220 K directly after the solid-solid transformation show no clear volume-pressure dependence, and were therefore not considered in the fit. Upon heating, relaxation occurred and a clear volume trend could be measured up to 262 K.

As represented in Figure S1 in the supporting information, some diffraction measurements were acquired beyond the stability range of some of the ices, taking advantage of the significant metastability at such low temperatures. Single crystals were formed at the melting curve to ensure pressure and temperature measurement accuracy.

2.2. Gibbs Energy Representation

A Gibbs energy surface for each ice polymorph was determined using (i) our new measurements of volumes as a function of pressure and temperature, (ii) thermal pressures calculated from quasi-harmonic phonon (vibrational) densities of state, (iii) reported elastic moduli measured as a function of pressure and temperature, (iv) estimates of the configurational entropy S_o and Gibbs energy G_o at a defined reference state, and (v) previously determined liquid-solid phase boundaries (i.e., melting curves).

Relationships between partial derivatives of Gibbs energy and the thermodynamic properties amenable to measurements (Table 1) provide a path for the determination of Gibbs energy. Using a chosen set of basis functions to represent the energy surface, and with Gibbs energy and derivatives of Gibbs energy specified at sufficient pressure-temperature points, model parameters can be readily determined by least-square fitting (a "collocation" solution of the differential properties). This numerical inverse problem is linear for Gibbs energy, entropy, volume, and specific heat. Iterations are required to match bulk moduli and thermal expansivity measurements.

Here, following the collocation methods described in Brown (2018), LBF representations are implemented using sixth order tensor b-splines. By construction, these basis functions are orthonormal and complete on the representational domain. The parameterization of the representations is universal. No material-specific coding is required and the representations can be readily modified in the face of new or improved measurements. Subroutines/functions are available in most standard scientific numerical environments currently in use. Examples are provided in the supporting information (Text S2).

In the following subsections we provide first the governing equations for the numerical evaluation of the Gibbs energy, followed by details on the Mie-Grüneisen equation of state to fit our pressure-volume temperature data, description of the vibrational energy physical model, and finally the adjustment strategy of all model parameters.

2.2.1. Governing Equations

The Gibbs energies for ices II, III, V, and VI at all relevant pressures and temperatures can be numerically evaluated through successive integrations, starting at reference values of G_o and S_o where the subscript typically denotes either absolute zero and ambient pressure or a specified thermodynamic invariant (e.g., a triple point).

$$G(P,T) = \int_{P_o}^{P} V(P,T)dP + G(P_o,T), \tag{1}$$

with $V(P,T)$ the specific volume and $G(P_o,T)$ the Gibbs energy temperature profile at ambient pressure. A Mie-Grüneisen equation of state (described hereafter) is used to represent $V(P,T)$, and the temperature dependence of Gibbs energy at the reference pressure is given as

$$G(P_o,T) = G_o(P_o,T_o) - S_o(P_o,T_o)\,(T-T_o) + \int_{T_o}^{T} C_P dT - T\int_{T_o}^{T} \frac{C_P}{T} dT. \quad (2)$$

The chosen values for G_o and S_o and for the (adjustable) parameters associated with the Mie-Grüneisen equation of state are discussed in section 2.2.4. The constant pressure specific heat, C_p, is determined from the constant volume specific heat, C_v, that is based on the quasi-harmonic phonon energy E_{vib} (described in section 2.2.3) and the derivatives of $V(P,T)$ that establish the isothermal bulk modulus, K_T, and thermal expansivity, α:

$$C_P = C_V(P,T) + V(P,T)\,TK_T(P,T)\,\alpha^2(P,T). \quad (3)$$

Next, from the numerical evaluation of the Gibbs energies, specific volumes, and heat capacities, an analytic LBF representations of Gibbs energy for each ice polymorph is then constructed by collocation (Brown, 2018). The smallest number of model parameters (number of control points for the splines) is found that allows an adequate fit of available data.

2.2.2. Mie-Grüneisen Equation of State

The Mie-Grüneisen equation of state (Davis, 1972) permits a physically motivated representation of specific volumes, valid over a wide range of pressures and temperatures, that is implemented using a small number of adjustable parameters. It has been used in condensed matter physics to provide reference equations of states of solids (e.g., for NaCl; Brown, 1999). The total pressure is separated into a static compression component (cold compression curve at 0 K) and a thermal component associated with lattice vibrations:

$$P(V,T) = P_{0K}(V) + P_{therm}(V,T). \quad (4)$$

Here the cold compression curve P_{0K} is described using third order Eulerian finite-strain formalism:

$$P_{0K} = 3K_o f_E(1+2f_E)^{5/2}\left(1+\frac{3}{2}(K_o'-4)f_E\right), \quad (5)$$

with the Eulerian strain given as $f_E = [(V_o/V)^{2/3} - 1]/2$, K_o and K_o' are the bulk modulus and its pressure derivative at 1 bar and 0 K.

The thermal pressure is

$$P_{therm} = \frac{\gamma}{V} E_{vib}(T,V), \quad (6)$$

where γ is the thermodynamic Grüneisen parameter and $E_{vib}(T,V)$ is the lattice vibrational energy. A power law volume dependence is assumed for the Grüneisen parameter:

$$\gamma(V) = \gamma_0 \left(\frac{V}{V_0}\right)^q. \quad (7)$$

Values for q between 1 and 2 are commonly used for solids under large range of compressions (Brown, 1999). Here for the very small pressure stability range and the associated small relative volume variation, a temperature-independent Grüneisen parameter with $q = 1$ is sufficient to adequately fit the data.

2.2.3. Vibrational Energy Model

The quasi-harmonic energy $E_{vib}(T,V)$ is computed using a phonon density of states (DoS) for each ice polymorph where $g(\nu, V)$ gives the number of modes lying in a frequency range between ν and $\nu+d\nu$. Ice, as a molecular solid, has nine degrees of freedom per molecule that naturally correlate with four families of modes, each with a distinct range of frequencies. These are translational modes (0–500 cm^{-1}), librational modes (500–1,100 cm^{-1}), bending modes (1,500–1,800 cm^{-1}), and stretching modes (3,200–3,800 cm^{-1}) with, respectively, 3, 3, 1, and 2 degrees of freedom. We use a combination of inelastic neutron scattering (INS) determinations for translational and librational modes of ices II, V, and VI (Li, 1996), and computed DoS where INS results are not available. A summary of the sources used in constructing the DoS, $g_{i,0}(\nu, V_0)$, for the four families at 0 K and 1 bar is presented in Table 2. As the INS data were obtained on quenched

Table 2
Details for the Constructed Ice Polymorphs Constructed Density of States

Ice polymorphs	Mode family	Type and conditions	Reference	γ_i	$\mathcal{N}_i$
Ice II	Translation	Measured INS/P = 20 mbar, T < 15 K	Li (1996)	1.3	3
	Libration	Measured INS/P = 20 mbar, T < 15 K	Li (1996)	0.5	3
	Bending	Computed (Q-TIP4P/F) /P = 0 Mpa, V_{ref} = 24.14 Å/molec.	Ramírez et al. (2012)	0.05	1
	Stretching	Computed (Q-TIP4P/F) /P = 0 Mpa, V_{ref} = 24.14 Å/molec.	Ramírez et al. (2012)	−0.15	2
Ice III	Translation	Computed (Q-TIP4P/F) /P = 0 Mpa, V_{ref} = 24.99 Å/molec.	Ramírez et al. (2012)	1.3	3
	Libration	Computed (Q-TIP4P/F) /P = 0 Mpa, V_{ref} = 24.99 Å/molec.	Ramírez et al. (2012)	0.25	3
	Bending	Computed (Q-TIP4P/F) /P = 0 Mpa, V_{ref} = 24.99 Å/molec.	Ramírez et al. (2012)	0.05	1
	Stretching	Computed (Q-TIP4P/F) /P = 0 Mpa, V_{ref} = 24.99 Å/molec.	Ramírez et al. (2012)	−0.1	2
Ice V	Translation	Measured INS/P = 20 mbar, T < 15 K	Li (1996)	1.6	3
	Libration	Measured INS P = 20 mbar, T < 15 K	Li (1996)	*1	3
	Bending	Computed/P = 0 Mpa, V_{ref} = 24.27 Å/molec	Jenkins and Morrison (2001)	*0	1
	Stretching	Computed/P = 0 Mpa, V_{ref} = 24.27 Å/molec	Jenkins and Morrison (2001)	−0.4	2
Ice VI	Translation	Measured INS/P = 20 mbar, T < 15 K	Li (1996)	2.5	3
	Libration	Measured INS/P = 20 mbar, T < 15 K	Li (1996)	*1	3
	Bending	Computed/P = 0 Mpa, V_{ref} = 20.88 Å/molec	Jenkins and Morrison (2001)	*0	1
	Stretching	Computed/P = 0 Mpa, V_{ref} = 20.88 Å/molec	Jenkins and Morrison (2001)	−0.44	2

samples at cryogenic temperature and because thermal expansion tends to zero at absolute zero, these DoS determinations are associated with the reference volume V_o.

For constant mode Grüneisen parameters, $\gamma_i = -\frac{d\ln\nu_i}{d\ln V}$, the volume dependences of phonon frequencies follow as

$$\nu_i(V) = \nu_i(V_o)\left(\frac{V_0}{V}\right)^{\gamma_i}, \tag{8}$$

which allows computation of the volume dependence of $g_i(\nu, V)$. Although modes within families of modes can have different γ_i, here a single value (listed in Table 2) is assumed for each of the four vibrational families. Limited data for ices and other solids (based primarily on Raman and infrared measurements) indicate broad trends with translational modes showing values for γ_i in a range from 1 to 2. In contrast, the internal stretching and bending bonds show little or negative changes in frequency with compression. Although the γ_i must depend on volume (compatible with that shown for the thermodynamic γ in equation (7)), the impact on ν_i is second order and can be neglected.

For ices II, V, and VI, translational and stretching modes γ_i are estimated from experimental insitu spectroscopic studies of Raman-active mode shifts with pressure (Minceva-Sukarova et al., 1984). Libration and bending are more challenging to observe in diamond anvil cells as they are masked by the diamond's first and second order Raman signal. As no experimental nor computational data exist for those, we chose to use the same approach used for ice Ih, for which the E_{vib} is already known in detail (Feistel & Wagner, 2006). For ice Ih, translation and libration from Li (1996) and computed bending and stretching from Jenkins and Morrison (2001) give a value of γ_i of 1 for libration and 0 for bending modes. This provides a description with less than 5% error for E_{vib}. For ices II and III, we used the mean Grüneisen associated with the computed DoS family (Ramírez et al., 2012).

The integral of each DoS mode family is normalized by its degrees of freedom $\mathcal{N}_i$, such that $\int g_i d\nu = \mathcal{N}_i$, and assembled into the final DoS as a sum of all mode families $g(\nu, V)$. The quasi-harmonic energy E_{vib} per molecule of H_2O is then computed as a function of temperature and volume:

$$E_{vib}(T, V) = \int \frac{h\nu}{\exp(h\nu/kT)-1}\, g(\nu, V)\, d\nu, \tag{9}$$

where k is Boltzmann's constant, h is Plank's constant, and the integral is over the full frequency range of the vibrational modes.

The isochoric specific heat is obtained as the temperature derivative of the vibrational energy at constant volume:

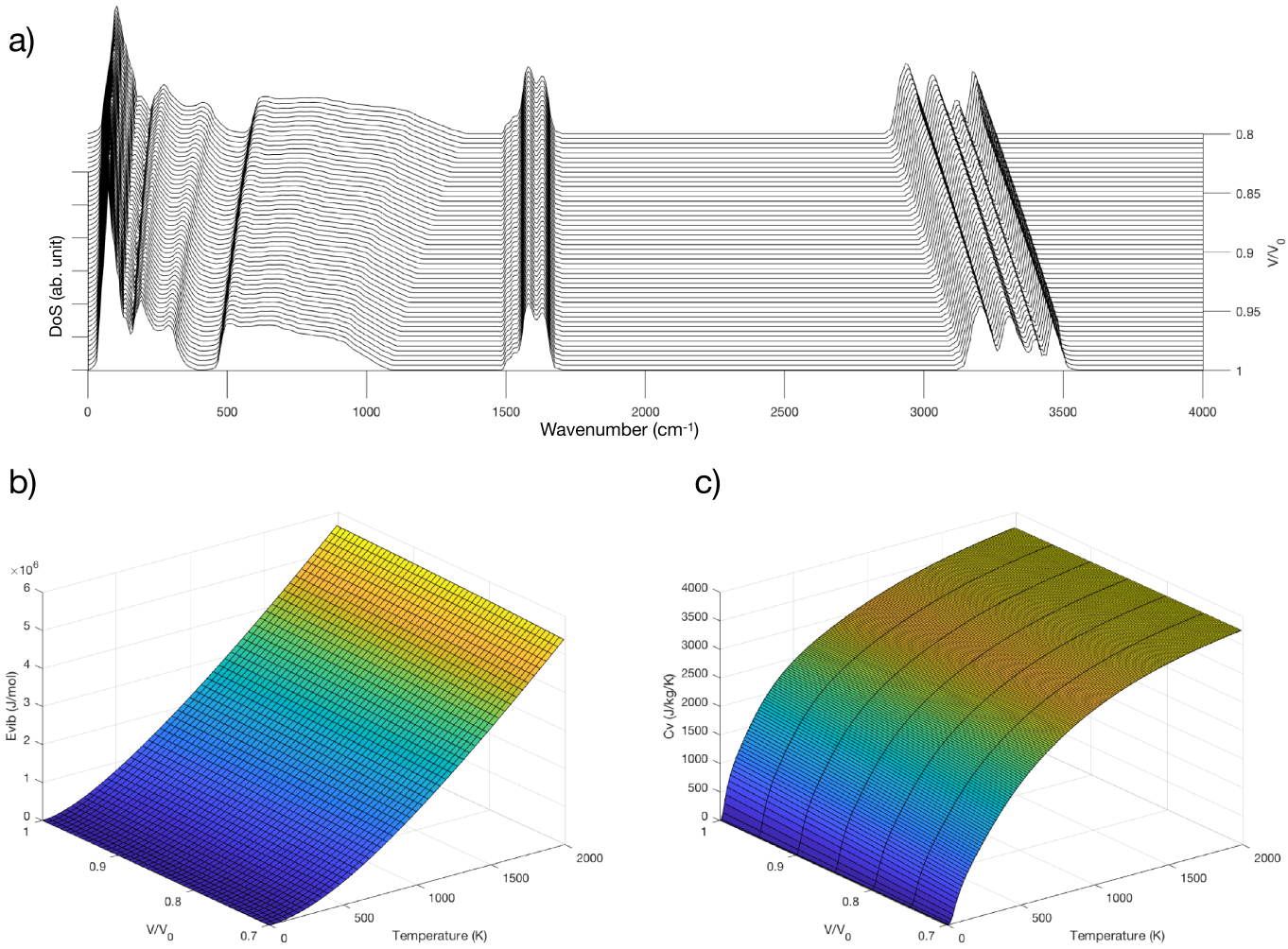

Figure 1. Thermal properties of ice V. (a) Phonon density of states as a function of frequency and volume compression, (b) vibrational energy E_{vib} as a function of compression and temperature, and (c) isochoric specific heat C_v as function of compression and temperature. Ices II, III, and VI thermal properties are provided in the supporting information (Figures S6–S8).

$$C_v = \left.\frac{\partial E_{vib}}{\partial T}\right|_V. \tag{10}$$

An example of a constructed DoS as a function of volume and resulting E_{vib} and C_v for ice V is shown in Figure 1. The densities of state for ices II, III, and VI are reported in the supporting information (Figures S6–S8).

In the range of temperatures associated with the equilibrium stability of these ices (<355 K), only translational and librational modes are sufficiently populated and contribute significantly to thermal properties. As necessary for the quasi-harmonic assumption, at high temperatures the model asymptotes to the Dulong-Petit limit for the C_v of water (4157.2 J/kg/K) (Figure 1). However, in the range of stability of these ices C_v is smaller and highly temperature dependent. Although explicit anharmonic contributions to the vibrational energy are likely at high temperatures, they are generally thought to be small in comparison with the harmonic contributions at modest or low temperatures and are ignored in the current analysis.

2.2.4. Adjustment of Model Parameters

For each ice phase, the four parameters (V_o, K_o, K_o', and γ_o) were adjusted to best fit both the volumes determined by means of diffraction measurements and the high-pressure determinations of the adiabatic bulk modulus based on ultrasonic and Brillouin measurements (Gagnon et al., 1988, 1990; Shaw, 1986; Shimizu et al., 1996; Tulk et al., 1997; Tulk et al., 1997).

Table 3
Ice Polymorphs Mie-Grüneisen Equations of States Fit Parameters

Phase	V_0 (m^3/kg)	V_0 (cm^3/mol)	K_o (GPa)	K'_o	γ_o	q
Ice II	$8.423 \cdot 10^{-4}$	15.17(5)	14.4(3)	6	1	1
Ice III	$8.595 \cdot 10^{-4}$	15.49(5)	9.9(3)	6	1.0	1
Ice V	$8.035 \cdot 10^{-4}$	14.48(5)	13.2(3)	6	1.1	1
Ice VI	$7.562 \cdot 10^{-4}$	13.62(2)	15.2(3)	6.5	1.4	1

In the IAPWS-95 representation of water (Wagner & Pruß, 2002), the internal energy and entropy are set to zero at its liquid-vapor-solid triple point. This convention was also adapted for the Gibbs energy representation of water by Bollengier et al. (2019) that provides more accurate thermodynamic properties at high pressures and in the supercooled regime. Here the reference energy G_o of each ice phase was set to be internally consistent with Bollengier et al. (2019) values by matching the Gibbs energy of the ice phase with water at each lower pressure triple point on the melt line (e.g., ice Ih-III-liquid triple point for ice III). For ice II, the reference energy G_o is set to be consistent with the computed Gibbs energy of ice III at the ice Ih-II-III triple point.

The entropy of the ices, important in determining the Clapeyron slopes, is the sum of a small "configurational" entropy associated with proton disorder (except for ice II which is proton ordered), as estimated by Herrero and Ramírez (2014), and a larger contribution from vibrational entropy. The latter was modified from initial estimates by small adjustments, within measurement and calculational uncertainties, to the frequencies of translational and libration modes (by factors of 1.01 to 1.07). These adjustments allowed a better match of melting points over the entire melting range of pressures for ices III, V, and VI. For ice II, adjustments were made to match Bridgman's (1912) determinations of the ice II–III solid-solid transition, assuming that hysteresis is negligible for this transition.

3. Results

3.1. X-Ray Diffraction Measurements

High-pressure low-temperature X-ray diffraction measurements of ice polymorphs were performed at the ID15B beamline (European Synchrotron Radiation Facility, France) using cryo-cooled diamond anvil cell. Ice powders of the forms II, III, V, and VI were obtained by freezing supercooled liquid water far from the melting line. Several volumes were obtained on unstrained single crystals annealed near the melting point. Volumes as a function of pressure were measured along several isotherms for each polymorph (Table 3). All powder and single crystal patterns could be fitted with the space groups R-3, $P4_12_12$, $C2/c$, and $P4_2/nmc$ for ices II, III, V, and VI, respectively. Examples of LeBail refinement are given in Figures S2, S3, S4, and S5 in the supporting information.

3.2. Thermodynamic Representations for Ice Polymorphs

3.2.1. Gibbs Energy Equation of State

Analytical Gibbs energy surfaces for ices II, III, V, and VI are derived using the methodology described above. Table 2 provides sources and data associated with the quasi-harmonic phonon densities of states and Table 3 lists equation of state parameters (K_o, K_o', V_o, and γ_o). Relevant constraints for G_o and S_o for each ice polymorph and the value in our models are reported in Table 4.

In Figure 2, pressures are shown as a function of volume for the four high-pressure ices. Based on the Mie-Grüneisen approach, measurements (filled symbols) minus calculated thermal (vibrational) pressures define "corrected" points (open symbols) that should lie within measurement uncertainty of the cold compression curve (dashed lines parameterized using K_o, K_o', and V_o). The 1-bar volumes for ice V and ice VI quenched to 98.15 K (Kamb, 1965) (the largest volume data for each ice) have relatively small thermal pressures and thus provide robust estimates of V_o. The quenched volume reported by Kamb for ices II and III are inconsistent with the current measurements and were excluded from the fit. For ice VI, our new cryogenic measurements at high pressure were combined with 45 points previously reported in Bezacier et al. (2014), ranging from 1,260 to 2,560 MPa and from 300 to 340 K, which were measured using the same experimental setup and procedures. The combined data cover the entire range of pressure stability of this polymorph. The thermodynamic Grüneisen parameters, γ_o, were chosen to be consistent with spectroscopically determined mode γ's (Table 2) and to reduce misfit of data on the cold compression curve. A systematic trend of larger γ_o values for higher pressure ices ranging from 1 to 1.4 is apparent in Tables 1 and 2.

The pressure derivative of the isothermal bulk modulus, K_o', is poorly constrained by volume measurements that span a relatively small range of compression. A value of 4 was assumed in the previous work of Fortes et al. (2012) and Bezacier et al. (2014). However, a strong constraint on the pressure dependence of the

Table 4
Experimental PVT Data

Ice II			Ice II (continued)		
Pressure (MPa)	Temperature (K)	Volume (Å^3)	Pressure (MPa)	Temperature (K)	Volume (Å^3)
370	180	298.11	410	200	298.96
330	180	298.38	260	220	300.85
320	180	298.62	240	220	301.27
320	180	298.97	320	220	300.5
280	200	300.19	370	220	299.75
340	200	299.75	280	240	302.19
380	200	299.37	280	240	302.64
Ice III			Ice III (continued)		
Pressure (MPa)	Temperature (K)	Volume (Å^3)	Pressure (MPa)	Temperature (K)	Volume (Å^3)
260	250.5	309.168	410	245.5	304.460
350	250.5	306.188	410	245.5	304.390
480	250.5	303.449	390	240.5	304.424
480	250.5	303.200	390	240.5	304.790
400	250.5	304.830	340	240.5	305.790
320	250.5	307.266	340	240.5	305.610
289	250.5	308.127	320	240.5	306.319
220	250.5	310.610	290	240.5	306.909
260	245.5	308.534	260	240.5	308.303
260	245.5	308.630	260	240.5	308.110
300	245.5	307.750	220	240.5	309.277
340	245.5	306.526	210	240.5	310.157
340	245.5	306.620	230	252.5	310.055
Ice V			Ice V (continued)		
Pressure (MPa)	Temperature (K)	Volume (Å^3)	Pressure (MPa)	Temperature (K)	Volume (Å^3)
689	242.3	654.867	566	252.3	660.269
562	242.3	660.141	578	249.3	660.479
531	242.3	662.162	581	243.3	659.901
496	242.3	663.845	583	237.3	659.206
421	242.3	667.471	581	232.3	659.638
506	262.3	665.551	603	222.3	658.473
538	262.3	663.699	647	222.3	656.677
548	262.3	663.103	704	222.3	654.532
500	252.3	664.129	779	222.3	651.850
Ice VI			Ice VI (continued)		
Pressure (MPa)	Temperature (K)	Volume (Å^3)	Pressure (MPa)	Temperature (K)	Volume (Å^3)
1,007	242.3	218.895	889	262.3	220.434
1,537	242.3	214.056	1,041	262.3	218.331
1,351	242.3	215.042	1,216	262.3	216.399
1,217	242.3	216.174	1,452	262.3	214.312
1,094	242.3	217.336	476	262.3	224.652
913	242.3	219.730	726	262.3	221.252
746	242.3	221.642	903	262.3	219.731
706	262.3	222.595			

Note. Typical uncertainties are estimated to be 30 MPa in pressure, 0.5 K in temperature, and $5{\cdot}10^{-3}$ Å^3 in volume.

adiabatic bulk modulus is provided by ultrasonic and Brillouin measurements (Gagnon et al., 1988, 1990; Shaw, 1986; Shimizu et al., 1996; Tulk, Gagnon, et al., 1997; Tulk, Kiefte, et al., 1997). Simultaneous fits to compressions (Figure 2) and the adiabatic moduli (Figure 3a**)** require that K_o' range from 6 for ice III and ice V to 6.5 for ice VI. To our knowledge, there are no previously published adiabatic bulk moduli versus pressure or temperature for ice II.

3.2.2. Shear Modulus and Seismic Velocities

The isotropic elastic shear modulus, μ, determined as the mean of Hashin-Shtrikman bounds (Brown, 2015) from single crystal measurements or directly from transverse wave speed measurements in isotropic polycrystalline samples (Gagnon et al., 1988, 1990; Shaw, 1986; Shimizu et al., 1996; Tulk, Gagnon, et al., 1997; Tulk, Kiefte, et al., 1997), are also shown in Figure 3a. A simple linear function in density and

Table 5
Values for the Triple Point Coordinates, Constraints to the Gibbs Energy Surface LBF Representations

	Triple point				Constrains values		LBF Gibbs representation values		
Phase	Triple point phases	P_{TP} (MPa)	T_{TP} (K)	Ref (TP)	$G_{ref}(P_{TP}, T_{TP})$ (Bollengier et al., 2019)	S_c	G_o (P_{TP}, T_{TP})	S_o (P_{TP}, T_{TP})	S_c
Ice II	Ih-II-III	213	238.5	Dunaeva et al. (2010)	$*1.8097 \cdot 10^5$	0	$3.9099 \cdot 10^5$	3516.4	0
Ice III	Ih-III-L	208.566	251.165	Wagner et al. (2011)	$1.9528 \cdot 10^5$	189.99	$4.3452 \cdot 10^5$	3326.4	189.99
Ice V	III-V-L	350.1	256.164	Wagner et al. (2011)	$3.2394 \cdot 10^5$	190.68	$5.7396 \cdot 10^5$	3327.7	190.68
Ice VI	V-VI-L	632.4	273.31	Wagner et al. (2011)	$5.7096 \cdot 10^5$	194.47	$8.4519 \cdot 10^5$	3346.5	194.47

Note. Configurational entropies S_c are from Herrero and Ramírez (2014). Gibbs energies are given in J kg^{-1} and entropies in J K^{-1} kg^{-1}. The $G_{ref}(P_{TP}, T_{TP})$ value for ice II, marked by an asterisk, is equal to the ice III Gibbs energy at the Ih-II-III triple point: $G_{iceIII}(P_{TP}, T_{TP})$.

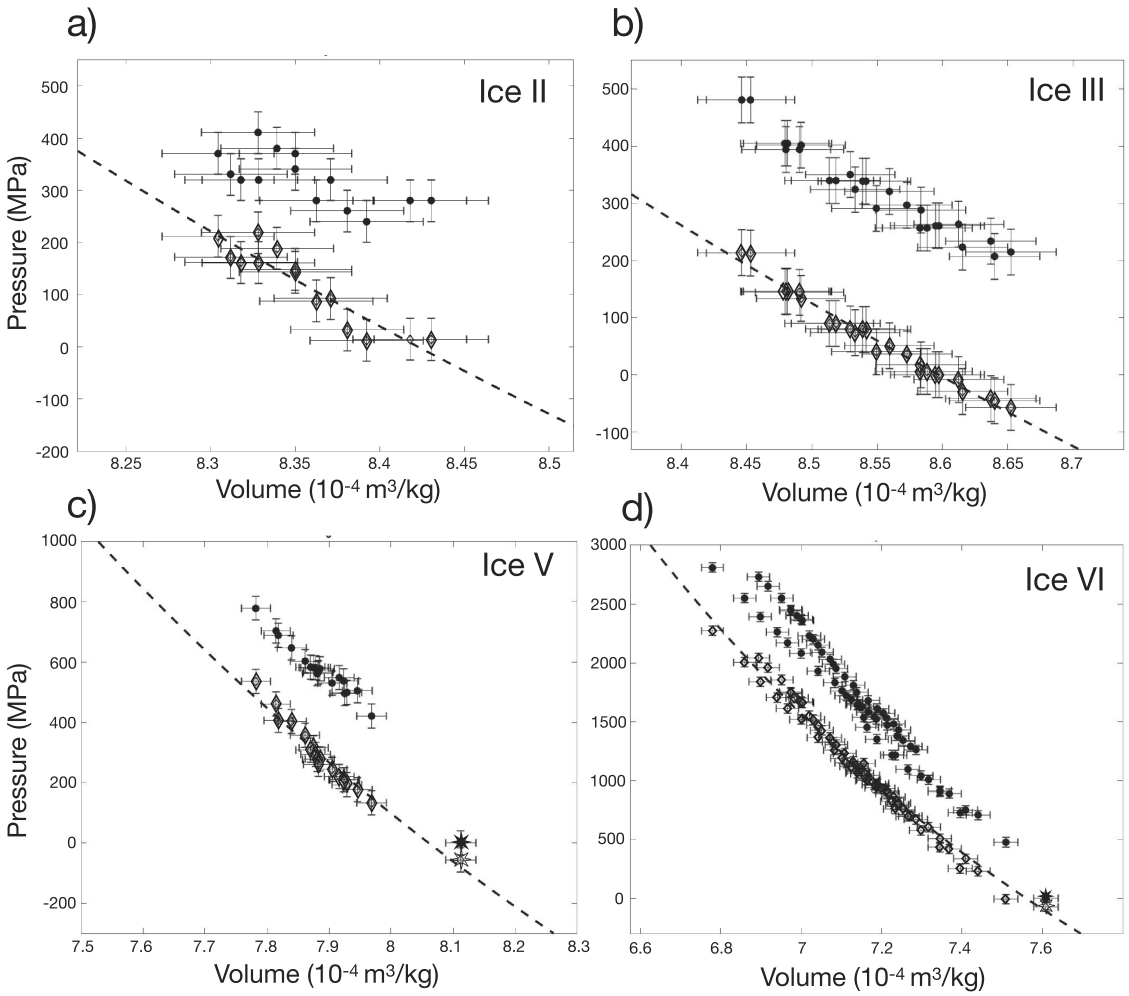

Figure 2. Pressures as a function of specific volume for (a) ice II, (b) ice III, (c) ice V, and (d) ice VI. Black filled symbols are measurements. White diamond symbols are measurements minus P_{therm} that provide an estimate of the zero-Kelvin compression curve. Stars for ice V and ice VI are the ambient pressure volumes from Kamb (1965). Experimental uncertainties are indicted as 30 MPa in pressure and 0.3% in volume. The dashed curves are the result fits of the cold-compression (zero-Kelvin) data.

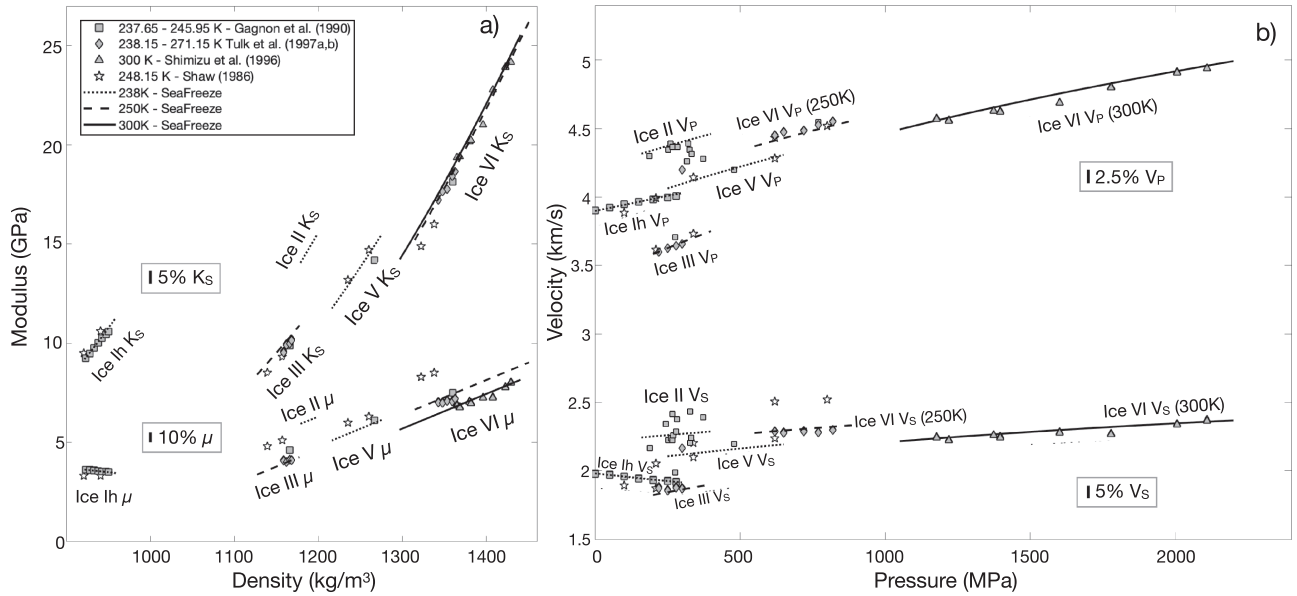

Figure 3. Isotropic aggregate elastic properties for ices Ih, II, III, V, and VI. (a) Bulk K_S and shear μ moduli as a function of density and (b) isotropic P and S waves velocities as a function of pressure. Different symbols (described in the legend) are used for data sets from different studies. Brillouin spectroscopy and sound speed data (Gagnon et al., 1988, 1990; Shaw, 1986; Shimizu et al., 1996; Tulk, Gagnon, et al., 1997; Tulk, Kiefte, et al., 1997). Solid (300 K), dashed (250 K), and dotted (238 K) lines are predictions based on the SeaFreeze representations. Vertical scales in gray boxes near the data are indicative of the typical scatter within one data set (5% in K_S, 10% in μ, 2.5% in V_P, and 5% in V_S).

temperature ($\mu = A + B^*\rho + C^*T$) using the same parameters adequately fits the shear moduli of high-pressure ices III, V, and VI, while different parameters were required for ice Ih (see details in Text S1 of the supporting information). Ice II shear moduli were fitted using a different A parameter to reproduce the sound speeds results from Gagnon et al. (1990) shown in Figure 3b. Density and temperature dependence were kept equal to the corresponding parameters for other high-pressure ices, as no data were available to provide other constrains. This results in a prediction of ice II shear modulus around 6 GPa at 238 K and 300 MPa. Using this parameterization and the adiabatic bulk modulus and density from the Gibbs energy representations, isotropic body wave velocities (compressional $V_P(P,T) = \sqrt{\left[K_S(P,T) + \frac{4}{3}\mu(P,T)\right]/\rho(P,T)}$ and transverse $V_S(P,T) = \sqrt{\frac{\mu(P,T)}{\rho(P,T)}}$) are compared as a function of pressure with measurements in Figure 3b. The computed sound speeds match most of the data within a few percent, with the exception of the shear wave velocities reported for ice VI by Shaw (1986).

3.2.3. Ice Polymorph Melting Curves

The predicted phase boundaries for both solid-liquid and solid-solid transitions from the intersections of Gibbs surfaces are shown in Figure 4 along with experimental determinations. Temperature residuals of data from the predicted melting points are plotted in Figure 5. The Gibbs energy for Ice Ih is a direct LBF parametrization of the Feistel and Wagner (2006) equation of state.

More than 90% of the reported melting points (including metastable determinations) lie within the measurement uncertainty of the Gibbs energy-determined melting lines. The current melting curve for ice V is indistinguishable from the Simon-Glatzel parameterization of Wagner et al. (2011). Although the ice III melting curve of Wagner et al. (2011) has larger curvature than the current prediction, both lie within the 0.6 K uncertainty range. Measurements of ice VI melting are well represented over a much larger range of pressure than for the other lower pressure polymorphs. The distinct curvature of the melting line shown in Figure 3 is well matched by the current representations, lending credence to the underlying physical model. Previously reported locations of the VI-VII-liquid triple point range from 352.2 to 355 K and from 2,160 to 2,216 MPa (Journaux et al., 2013; Wagner et al., 2011). Using Wagner et al. (2011) Simon-Glatzel parameterization for the ice VII melting curve, our estimated VI-VII-L triple point at 353.5 K and 2,200 MPa lies within the prior bounds.

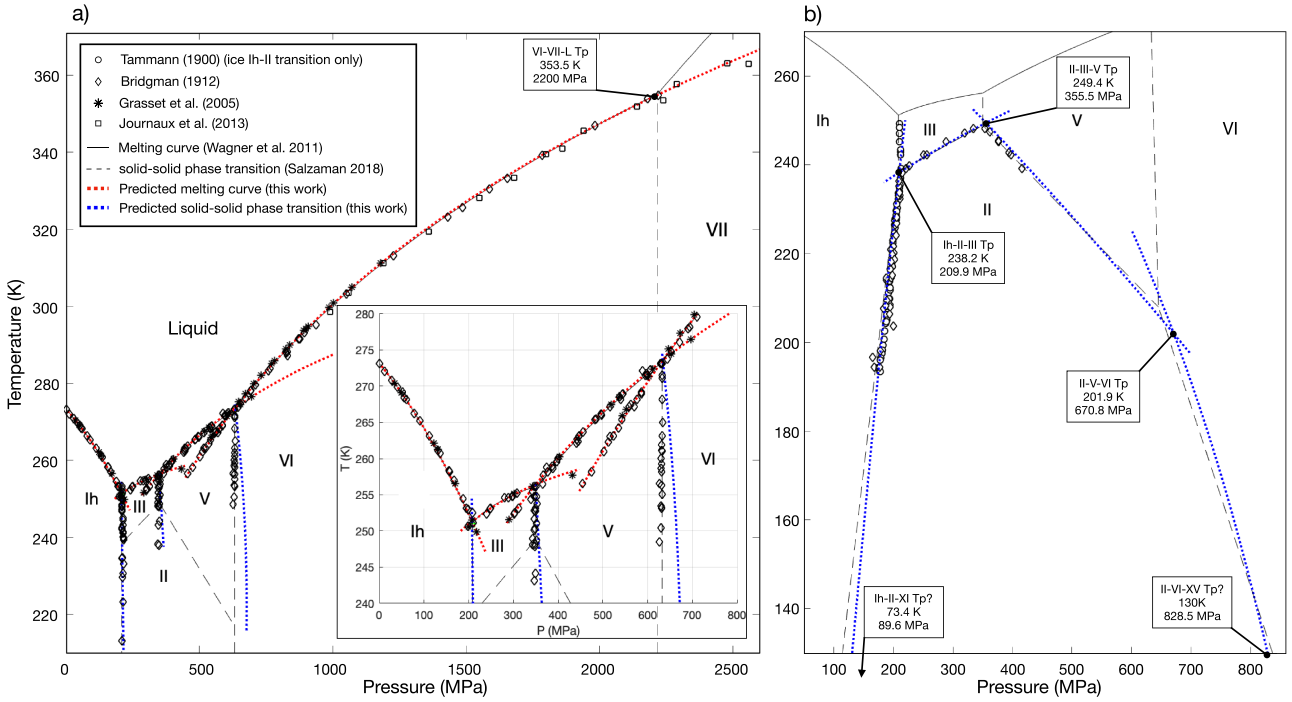

Figure 4. Water phase diagram. (a) Ices polymorphs melting curves and Ih–III, III–V, and V–VI solid-solid phase transitions calculated using the Gibbs LBF representations in red and blue dotted lines, respectively. Melting curves from the Simon-Glatzel equations for the melting curves from Wagner et al. (2011), represented with a thin black line, often overlap by the LBF predicted melting lines at this scale. Solid-solid phase transitions from Bridgman (1912) are represented as dashed black lines. Experimental data are represented as open diamonds from Bridgman (1912) and Bridgman (1937), black asterisks from Grasset et al. (2005), open squares from Journaux et al. (2013), and open circles for Kell and Whalley (1968). A zoom on the ice Ih-III-V melting region is shown on the bottom right. (b) Ice II stability field with data from Bridgman (1912) and Tammann (1900) (systematic error in pressure corrected to agree with Bridgman), solid-solid phase transitions and position of predicted triple points (Tp).

3.2.4. New Predictions of Solid-Solid Phase Transitions and Triple Points

The solid-solid phase transitions for ices Ih–III, III–V, and V–VI are model predictions, since no optimization was undertaken to match these transitions. As shown in Figure 3, the predicted ice Ih–ice III transition matches measurements while the predicted ice III–ice V and ice V–ice VI transitions are systematically offset by up to 30 MPa. The Ih–III transition was determined (Bridgman, 1912; Kell & Whalley, 1968) in reversed measurements, crossing the boundary during both compression and decompression. In contrast, the determinations for ice III–ice V and ice V–ice VI by Bridgman (1912) represent pressures of transition during decompression only. Based on normal hysteresis of solid-solid transitions requiring significant structural reorganizations, it is likely that such measurements would significantly underestimate the transition pressure. For example, Pistorius et al. (1968) reported 100 MPa of hysteresis for the ice VI–VII transition. We suggest that our estimates for the solid-solid transitions better represent thermodynamic equilibrium than determinations based on unreversed measurements.

The ice II parameterization reproduces the previously published results for Ih–II, II–III, and II–V transition within experimental uncertainties (<10 MPa) (Bridgman, 1912; Tammann, 1900). Although the II–VI transition has not been experimentally observed (Salzmann, 2018), the present Gibbs parametrization (Figure 4b) predicts the ice II-V-VI triple point to lie at 209.1 K and 670.8 MPa. Since our representation is based on a robust physical model for the thermal energy, low temperature predictions should remain valid for the ice VI–ice XV (proton ordering) transition at 130 K (Salzmann et al., 2009). Based on observed temperatures of transition for XI–Ih (Yen & Chi, 2015) and XV–VI (Salzmann et al., 2009), we predict a Ih-II-XI triple point at 73.4 K & 89.6 MPa and a II-VI-XV at 130 K and 828.5 MPa.

3.2.5. Metastable and Equilibrium Thermodynamic Properties for Icy World Interiors

The current Gibbs energy representations are expected to sensibly predict properties both within and beyond the stability range of each ice phase. An illustration of thermodynamic properties

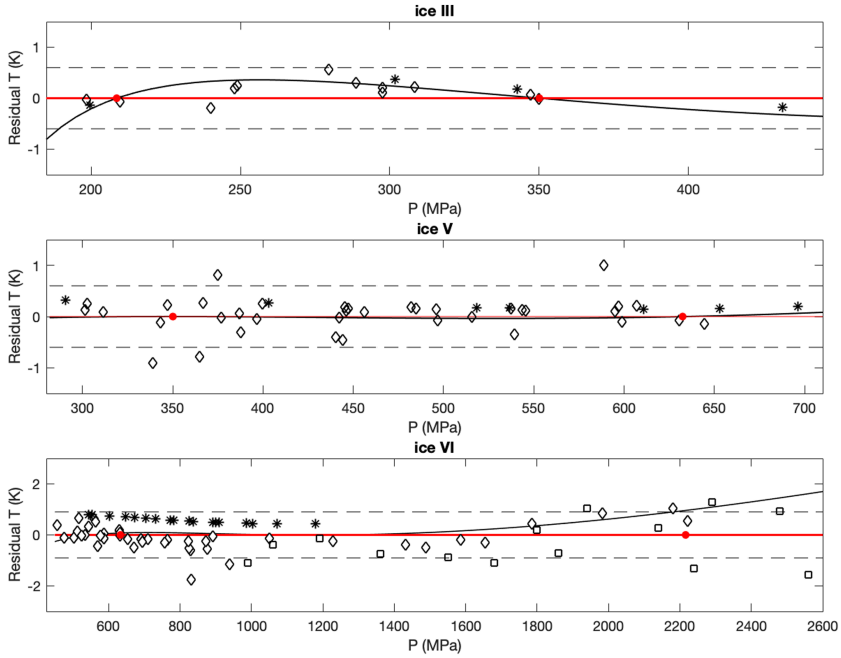

Figure 5. Temperature residuals of the melting curves data (see Figure 3 for symbols references) and the Simon-Glatzel equations from Wagner et al. (2011) as black lines, with our LBF-calculated melting boundaries (red line). Propagated temperature uncertainties of 0.6 K for ice III and ice V and 0.9 K for ice VI (corresponding to the reported pressure and temperature uncertainties) are represented as black dashed lines. Triple points from Wagner et al. (2011) are represented as red dots.

determination for ice V is presented in Figure 6, over a wide range of temperatures and pressures. Other polymorphs and liquid water thermodynamic surfaces are provided in Figures S9–S12 in the supporting information. All surfaces extrapolate with reasonable trends into the metastable regions and have correct limiting behavior at absolute zero where thermal expansivity and specific heat go to zero. Since the characteristic temperatures of molecular vibrational modes (libration, bending, and stretching) are high, specific heat remains temperature dependent and, in the stability field of ice V, is approximately half the high-temperature Dulong-Petit limit (4157.2 J/kg/K). The only other specific heat estimations for high pressure ice derived by Tchijov (2004), following on the ice VII calculations of Fei et al. (1993), are up to 35% higher than the current analysis. Their use of the Debye approximation (inappropriate for molecular solids like ices) does not adequately account for the large number of high frequency molecular modes.

Figure 7 depicts the behavior with pressure of major thermodynamic properties (density, thermal expansivity, specific heat, and isothermal bulk modulus) computed using the LBF representations and seismic velocities for ices Ih, III, V, and VI. These are provided up to 2,300 MPa, on isotherms relevant to the interiors of icy ocean worlds, at 250, 260, 270, and 300 K (Lunine, 2017; Sohl et al., 2010; Vance, Planning, et al., 2018). Temperature has a notable effect only on specific heat and thermal expansivity which shows 20% to 30% increases with increasing temperature in this 50 K range. However, over the relevant pressure range, all changes in thermodynamic parameters and seismic wave velocities show significant variations with pressure and with the solid-solid phase transitions. Ice II is not represented here for clarity as its stability at <250 K limits its importance for larger icy moons interiors. Its thermodynamic properties surfaces are reported in Figure S12 in the supporting information.

3.2.6. The "SeaFreeze" Thermodynamic Framework

The LBF Gibbs surfaces of ices II, III, V, and VI are combined with the liquid water representation of Bollengier et al. (2019), and the representation for ice Ih (Feistel & Wagner, 2006) (converted to the LBF format) as the open source computational tool "SeaFreeze" (in Python and Matlab™) that is provided in a GitHub repository (https://github.com/Bjournaux/SeaFreeze). The SeaFreeze representations are thermodynamically consistent within and between phases. Gibbs energies and entropies of all phases are referenced to

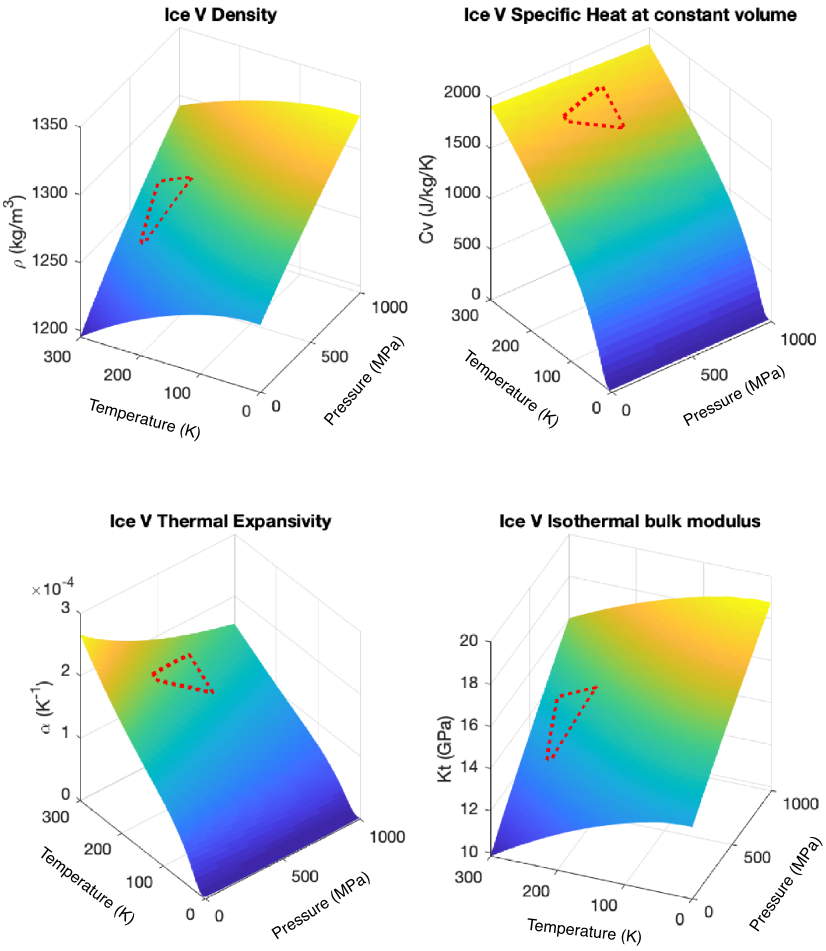

Figure 6. Thermodynamic properties of ice V determined as derivatives of the LBF representation of Gibbs energy inside and beyond its stability range (red dashed lines).

IAPWS-95 values for water at its vapor-fluid-ice Ih triple point (Bollengier et al., 2019). This tool gives equilibrium thermodynamic properties (including phase boundaries, density, heat capacities, bulk modulus, thermal expansivity, chemical potentials) as well as shear moduli and seismic wave velocities for each phase extending into metastable regimes. Details and examples on using SeaFreeze is provided in the Text S2 in the supporting information.

The SeaFreeze implementation is computationally efficient. More than 10^5 thermodynamic points per second can be determined on a mid-range 2015-vintage laptop computer (2.7GHz Intel core i5-5257U CPU). Thus, use of SeaFreeze within computationally intensive frameworks (e.g., geodynamic simulations) appears possible.

4. Discussion and Perspectives

A uniform numerical environment for the thermodynamic properties of water and phases in equilibrium with water from ambient to high pressures supports research in a broad range of fields including astrobiology, planetary sciences, oceanic science, geochemistry, and condensed-matter physics. Planetary interior studies have illustrated the importance of using thermodynamically consistent properties of hydrosphere materials in icy ocean worlds (Mitri et al., 2014; S. Vance et al., 2014; Vance, Panning, et al., 2018) while also noting inconsistencies in available parameterizations. SeaFreeze offers clarity in how measurements inform the representations and consistency in how properties relate to energy and entropy reference states. The transparency of the open source process creates an opportunity to improve and extend the framework with

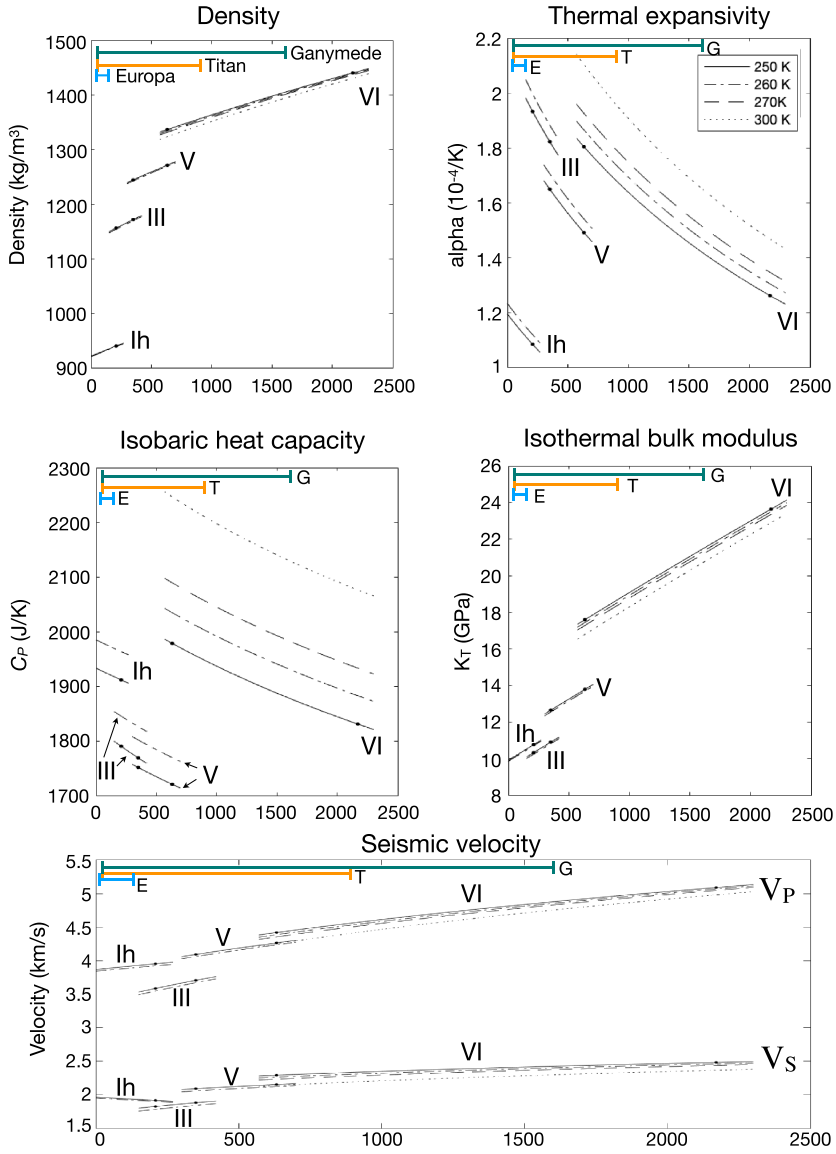

Figure 7. Thermodynamic properties and seismic velocities for ice Ih, III, V, and VI based on the SeaFreeze parameterizations. Isotherms at 250, 260, 270, and 300 K are shown. The estimated pressure range found in the hydrosphere of Europa (E), Titan (T), and Ganymede (G) are reported as blue, yellow, and green bars, respectively (Vance, Planning, et al., 2018). Black dots on the 250 K profile represent the equilibrium pressure for the solid-solid phase transitions.

future data. Other ice phases can be included to extend the range of applications (e.g., ice VII, ice X, and additional stable or metastable ice polymorphs). The framework can also be extended to accommodate major planetary solutes, including solid phases of interest for planetary hydrospheres, such as salts and hydrates. Representations for electrolyte solutions are under development. Not included at this time in SeaFreeze are transport properties such as thermal and electrical conductivities, viscosities of fluids, and rheological properties of solids. These could also find a place within the SeaFreeze framework.

For conditions found inside icy ocean worlds (0–1,800 MPa, 150–350 K), pressure changes and solid-solid phase transitions are the dominant factors for changes in thermodynamic properties and seismic wave velocities of ices (Figure 7). The temperature range expected in these planetary bodies being more limited, only the specific heat and the thermal expansivity are significantly altered for all ice polymorphs.

Prior studies of the interiors and geodynamics of icy moons and water-rich planets (e.g., Noack et al., 2016; Choblet et al., 2017; Kalousová et al., 2018; Marounina & Rogers, 2019) relied on ad hoc thermodynamic

parameterizations with tenuous physical bases, built from limited data. The present framework, using accurate and self-consistent descriptions of the candidate constituents, will significantly aid investigations of the icy moon interiors and their potential habitability. As an example, the presently estimated heat capacities of high-pressure ices being 20–35% smaller than previously predicted ones (Tchijov, 2004), the resulting adiabatic gradient in the high-pressure ice mantle of icy worlds should significantly increase. This could lead to an increase in the estimated heat flux toward the ocean of a similar magnitude, with all other parameters kept equal.

Looking beyond our solar system, the representation reported here encompassing all ice polymorphs and liquid water up to 2,300 MPa is also relevant for the study of exoplanets interiors and their potential habitability. This is especially true for water worlds like the ones proposed in the TRAPPIST-1 system (Grimm et al., 2018; Unterborn et al., 2018). The self-consistent thermodynamic properties for water and its ices provided by SeaFreeze can be used to accurately study the interior structure and evolution of watery exoplanets (Noack et al., 2016), computing of radius-mass curves (Sotin & Grasset, 2007; Unterborn et al., 2018), as well as studying their habitability and the effects of possible snow-ball regime on ocean words (Kite & Ford, 2018; Ramirez & Levi, 2018). It should be noted that these world's hydrospheres could be significantly thicker than those of large icy moons, resulting in possibly ice VII and ice X being present as well. The validity of the present SeaFreeze representations extends to ice VI (2,300 MPa). Ice VII and ice X representations will be included in future revisions.

The scientific objectives of upcoming flagship missions (NASA Europa Clipper, Phillips & Pappalardo, 2014; and ESA/JUICE, Grasset et al., 2013) include a strong emphasis on the study of water-rich planetary interiors and the potential habitability of icy moons. Instrument investigations planned for these missions will determine gravitational moments and induced magnetization that depend on high-pressure aqueous system thermodynamics (Vance, Planning, et al., 2018, and reference therein).

The recent success of the Mars InSight seismometer on the Martian surface highlights the importance of seismic investigations to determine planetary structure. Two concept lander missions, a Europa Lander (Hand, 2017; Pappalardo et al., 2013) and the recently selected New Frontiers Dragonfly mission to Saturn's moon Titan (Ralph D Lorenz et al., 2018), include a seismometer package. Because SeaFreeze body wave velocities in ices and fluids can be implemented in seismic models (Panning et al., 2018; Stähler et al., 2018, 2019), this framework can be used to refine seismic instrument specifications, and ultimately can be a resource for the analysis of mission data.

In summary, using state of the art techniques, we accurately measured long-needed volumes of H_2O ices II, III, V, and VI over 180–270 K and 200–1,600 MPa, within and beyond their stability fields. By combining these data with a physically grounded thermal model to determine the Gibbs energy, we provide the first Gibbs energy equations of state for ices II, III, V, and VI. These Gibbs representations allow accurate determination of melting curves (including metastable extensions) to 2,300 MPa. Moreover, our vibrational energies, based on a statistical physics and experimental and computational densities of state for each polymorph, allow us to derive for the first time physically grounded specific heats for ices II, III, V, and VI. Our comprehensive Gibbs representations refine the solid-solid phase boundaries down to 130 K (Ih–II, Ih–III, II–III, II–V, II–VI, III–V, V–VI), identifying the hysteresis in the unreversed measurements of Bridgman (1912). We combined these Gibbs representation in an open source and modular computational framework “SeaFreeze” (in Python and Matlab™), providing access to thermodynamic properties of water and ices under conditions found in the hydrospheres of ocean worlds.

Author Contributions

BJ is the leading author of this manuscript. BJ and JMB wrote the manuscript with input from all authors. BJ, AP, IC, SP, TBB, SV, and JO operated the high-pressure X-ray diffraction experiments at the ID-15B beamline of the European Synchrotron Radiation Facility, Grenoble, France, with the scientific and technical support of FC, GG, and MH. AP, IC, and TBB analyzed the X-ray diffraction data. BJ and JMB developed and produced the Gibbs energy equations of state for the ice polymorphs, based on the LBF framework developed by JMB. The open source SeaFreeze code was written in MATLAB and Python by BJ, PE, and JMB.

Data Availability Statement

The SeaFreeze open-access code is available at https://doi.org/10.5281/zenodo.3367730, an open source repository hosted by Zenodo (all results presented here are computed using the released version 0.9.2). Future updates will be available through GitHub (https://github.com/Bjournaux/SeaFreeze). See the supporting information Figure S1 for data PT coordinates and Figures S2–S5 for examples of LeBail refinement of high-pressure ices II, III, V, and VI X-Ray diffraction patterns. In Figures S6–S8, constructed phonon density of states and resulting thermal energy and isochoric specific heat are represented for ice II, III, and VI. Text S1 summarizes the fitting of the shear modulus and seismic wave data. Figures S9–S12 show the thermodynamic properties surfaces of ices II, III, and VI. Finally, Text S2 provides details and examples on how to use the SeaFreeze code.

Acknowledgments
The authors acknowledge the financial support provided by the NASA Postdoctoral Program fellowship awarded to BJ. BJ, JMB, and SV were supported by the NASA Solar System Workings grant 80NSSC17K0775, by the Icy Worlds, and Habitability of Hydrocarbon Worlds: Titan and Beyond nodes of NASA's Astrobiology Institute (08-NAI5-0021 and 17-NAI8-2-017). Synchrotron radiation experiments were conducted under two beamtimes granted to BJ at the ID-15B beamline (proposals number: ES640 & ES807) at the European Synchrotron Radiation Facility, Grenoble, France. JO financial support was provided by the Department of Earth and Space Science of the University of Washington, Seattle, United States. TBB acknowledge financial support provided by the DFG grant BO-2550/8-1. Work by SDV was carried out at the Jet Propulsion Laboratory, California Institute of Technology, under a contract with the National Aeronautics and Space Administration (80NM0018D0004). The authors would like to thank Evan Abramson, Olivier Bollengier, Gabriel Tobie, and Christophe Sotin for the fruitful scientific discussions that greatly helped enhancing the quality of this work.

References

Bezacier, L., Journaux, B., Perrillat, J.-P., Cardon, H., Hanfland, M., & Daniel, I. (2014). Equations of state of ice VI and ice VII at high pressure and high temperature. *Journal of Chemical Physics*, *141*(10), 104505. https://doi.org/10.1063/1.4894421

Bollengier, O., Brown, J. M., & Shaw, G. H. (2019). Thermodynamics of pure liquid water: Sound speed measurements to 700 MPa down to the freezing point, and an equation of state to 2300 MPa from 240 to 500 K. *The Journal of Chemical Physics*, *151*(5), 054501. https://doi.org/10.1063/1.5097179

Bridgman, P. W. (1912). Water, in the liquid and five solid forms, under pressure. *Feistel*, *47*(13), 441–558. https://doi.org/10.2307/20022754

Bridgman, P. W. (1937). The phase diagram of water to 45,000 kg/cm^2. *The Journal of Chemical Physics*, *5*(12), 964–966. https://doi.org/10.1063/1.1749971

Brown, J. M. (1999). The NaCl pressure standard. *Journal of Applied Physics*, *86*(10), 5801–5808. https://doi.org/10.1063/1.371596

Brown, J. M. (2015). Determination of Hashin-Shtrikman bounds on the isotropic effective elastic moduli of polycrystals of any symmetry. *Computers & Geosciences*, *80*, 95–99. https://doi.org/10.1016/j.cageo.2015.03.009

Brown, J. M. (2018). Local basis function representations of thermodynamic surfaces: Water at high pressure and temperature as an example. *Fluid Phase Equilibria*, *463*, 18–31. https://doi.org/10.1016/j.fluid.2018.02.001

Choblet, G., Tobie, G., Sotin, C., Kalousová, K., & Grasset, O. (2017). Heat transport in the high-pressure ice mantle of large icy moons. *Icarus*, *285*, 252–262.

Choukroun, M., & Grasset, O. (2007). Thermodynamic model for water and high-pressure ices up to 2.2 GPa and down to the metastable domain. *The Journal of Chemical Physics*, *127*(12), 124506. https://doi.org/10.1063/1.2768957

Choukroun, M., & Grasset, O. (2010). Thermodynamic data and modeling of the water and ammonia-water phase diagrams up to 2.2 GPa for planetary geophysics. *The Journal of Chemical Physics*, *133*(14), 144502–144502–13. https://doi.org/10.1063/1.3487520

Coelho, A. A. (2018). TOPAS and TOPAS-Academic: An optimization program integrating computer algebra and crystallographic objects written in C++. *Journal of Applied Crystallography*, *51*(1), 210–218. https://doi.org/10.1107/S1600576718000183

Davis, R. O. (1972). Thermodynamic response of Mie-Grüneisen materials at high pressures. *Physik Der Kondensierten Materie*, *15*(3), 230–236. https://doi.org/10.1007/BF02422683

Dunaeva, A. N., Antsyshkin, D. V., & Kuskov, O. L. (2010). Phase diagram of H_2O: Thermodynamic functions of the phase transitions of high-pressure ices. *Solar System Research*, *44*(3), 202–222. https://doi.org/10.1134/S0038094610030044

Fei, Y., Mao, H., & Hemley, R. J. (1993). Thermal expansivity, bulk modulus, and melting curve of H_2O–ice VII to 20 GPa. *The Journal of Chemical Physics*, *99*(7), 5369–5373. https://doi.org/10.1063/1.465980

Feistel, R., & Wagner, W. (2006). A new equation of state for H_2O ice Ih. *Journal of Physical and Chemical Reference Data*, *35*(2), 1021–1047. https://doi.org/10.1063/1.2183324

Fortes, A. D., Wood, I. G., Alfredsson, M., Vočadlo, L., & Knight, K. S. (2005). The incompressibility and thermal expansivity of D_2O ice II determined by powder neutron diffraction. *Journal of Applied Crystallography*, *38*(4), 612–618. https://doi.org/10.1107/S0021889805014226

Fortes, A. D., Wood, I. G., Tucker, M. G., & Marshall, W. G. (2012). The P–V–T equation of state of D_2O ice VI determined by neutron powder diffraction in the range $0 < P < 2.6$ GPa and $120 < T < 330$ K, and the isothermal equation of state of D_2O ice VII from 2 to 7 GPa at room temperature. *Journal of Applied Crystallography*, *45*(3), 523–534. https://doi.org/10.1107/S0021889812014847/ks5309sup1.pdf

Gagnon, R. E., Kiefte, H., Clouter, M. J., & Whalley, E. (1988). Pressure dependence of the elastic constants of ice Ih to 2.8 kbar by Brillouin spectroscopy. *The Journal of Chemical Physics*, *89*(8), 4522–4528. https://doi.org/10.1063/1.454792

Gagnon, R. E., Kiefte, H., Clouter, M. J., & Whalley, E. (1990). Acoustic velocities and densities of polycrystalline ice Ih, II, III, V, and VI by Brillouin spectroscopy. *The Journal of Chemical Physics*, *92*(3), 1909. https://doi.org/10.1063/1.458021

Grasset, O., Amiguet, E., & Choukroun, M. (2005). Pressure measurements within optical cells using diamond sensors: Accuracy of the method below 1 GPa. *High Pressure Research*, *25*(4), 255–265. https://doi.org/10.1080/08957950500466018

Grasset, O., Dougherty, M. K., Coustenis, A., Bunce, E. J., Erd, C., Titov, D., et al. (2013). JUpiter ICy moons Explorer (JUICE): An ESA mission to orbit Ganymede and to characterise the Jupiter system. *Planetary and Space Science*, *78*, 1–21. https://doi.org/10.1016/j.pss.2012.12.002

Grimm, S. L., Demory, B.-O., Gillon, M., Dorn, C., Agol, E., Burdanov, A., et al. (2018). The nature of the TRAPPIST-1 exoplanets. *Astronomy & Astrophysics*, *613*, A68. https://doi.org/10.1051/0004-6361/201732233

Hand, K. P. (2017). *Report of the Europa Lander science definition team*. National Aeronautics and Space Administration.

Hanslmeier, A. (2011). *Water in the Universe*. Springer Science+Business Media.

Hendrix, A. R., Hurford, T. A., Barge, L. M., Bland, M. T., Bowman, J. S., Brinckerhoff, W., et al. (2019). The NASA roadmap to ocean worlds. *Astrobiology*. https://doi.org/10.1089/ast.2018.1955

Hernandez, J.-A., & Caracas, R. (2018). Proton dynamics and the phase diagram of dense water ice. *The Journal of Chemical Physics*, *148*(21), 214501. https://doi.org/10.1063/1.5028389

Hernandez, J.-A., & Caracas, R. (2016). Superionic-superionic phase transitions in body-centered cubic H_2O ice. *Physical Review Letters*, *117*(13), 135503. https://doi.org/10.1103/PhysRevLett.117.135503

Herrero, C. P., & Ramírez, R. (2014). Configurational entropy of hydrogen-disordered ice polymorphs. *The Journal of Chemical Physics*, *140*(23), 234502. https://doi.org/10.1063/1.4882650

Jenkins, S., & Morrison, I. (2001). The dependence on structure of the projected vibrational density of states of various phases of ice as calculated by ab initio methods. *Journal of Physics: Condensed Matter*, *13*(41), 9207. https://doi.org/10.1088/0953-8984/13/41/312

Journaux, B., Daniel, I., Caracas, R., Montagnac, G., & Cardon, H. (2013). Influence of NaCl on ice VI and ice VII melting curves up to 6 GPa, implications for large icy moons. *Icarus*, *226*(1), 355–363. https://doi.org/10.1016/j.icarus.2013.05.039

Journaux, B., Daniel, I., Petitgirard, S., Cardon, H., Perrillat, J.-P., Caracas, R., & Mezouar, M. (2017). Salt partitioning between water and high-pressure ices. Implication for the dynamics and habitability of icy moons and water-rich planetary bodies. *Earth and Planetary Science Letters*, *463*, 36–47. https://doi.org/10.1016/j.epsl.2017.01.017

Kalousová, K., Sotin, C., Choblet, G., Tobie, G., & Grasset, O. (2018). Two-phase convection in Ganymede's high-pressure ice layer — Implications for its geological evolution. *Icarus*, *299*, 133–147.

Kamb, B., Prakash, A., & Knobler, C. (1967). Structure of ice. V. *Acta Crystallographica*, *22*(5), 706–715. https://doi.org/10.1107/S0365110X67001409

Kamb, B. (1965). Structure of ice VI. *Science*, *150*(3693), 205–209. https://doi.org/10.1126/science.150.3693.205

Kamb, B., & Davis, B. L. (1964). Ice VII, the densest form of ice. *Proceedings of the National Academy of Sciences of the United States of America*, *52*(6), 1433–1439. https://doi.org/10.1073/pnas.52.6.1433

Kell, G. S., & Whalley, E. (1968). Equilibrium line between ice I and III. *Journal of Chemical Physics*, *48*, 2359–2361. https://doi.org/10.1063/1.1669437

Kite, E. S., & Ford, E. B. (2018). Habitability of exoplanet waterworlds. *The Astrophysical Journal*, *864*(1), 75. https://doi.org/10.3847/1538-4357/aad6e0

Léger, A., Selsis, F., Sotin, C., Guillot, T., Despois, D., Mawet, D., et al. (2004). A new family of planets? *Icarus*, *169*(2), 499–504. https://doi.org/10.1016/j.icarus.2004.01.001

Li, J. (1996). Inelastic neutron scattering studies of hydrogen bonding in ices. *The Journal of Chemical Physics*, *105*(16), 6733–6755. https://doi.org/10.1063/1.472525

Lobban, C., Finney, J. L., & Kuhs, W. F. (2002). The p–T dependency of the ice II crystal structure and the effect of helium inclusion. *The Journal of Chemical Physics.*. https://doi.org/10.1063/1.1495837

Lobban, C., Finney, J. L., & Kuhs, W. F. (2000). The structure and ordering of ices III and V. *The Journal of Chemical Physics.*. https://doi.org/10.1063/1.481282

Londono, J. D., Kuhs, W. F., & Finney, J. L. (1998). Neutron diffraction studies of ices III and IX on under-pressure and recovered samples. *The Journal of Chemical Physics.*. https://doi.org/10.1063/1.464942

Lorenz, R. D., Panning, M., Stahler, S., Shiraishi, H., Yamada, R., & Turtle, E. P. (2019). Titan Seismology with Dragonfly: Probing the Internal Structure of the Most Accessible Ocean World. In *Lunar and Planetary Science Conference* (Vol. 50, p. 2173).

Lorenz, R. D., Turtle, E. P., Barnes, J. W., & Trainer, M. G. (2018). Dragonfly: A rotorcraft lander concept for scientific exploration at Titan. *Johns Hopkins APL Technical Digest*, *34*(3), 14.

Lunine, J. I. (2017). Ocean worlds exploration. *Acta Astronautica*, *131*, 123–130. https://doi.org/10.1016/j.actaastro.2016.11.017

Marounina, N., & Rogers, L. A. (2019). Internal Structure and CO2 Reservoirs of Habitable Water-Worlds. *arXiv:1904.10458 [astro-ph]*.

McFarlan, R. L. (1936a). The structure of ice II. *The Journal of Chemical Physics*, *4*(1), 60–64. https://doi.org/10.1063/1.1749748

McFarlan, R. L. (1936b). The structure of ice III. *The Journal of Chemical Physics*, *4*(4), 253–259. https://doi.org/10.1063/1.1749832

Minceva-Sukarova, B., Sherman, W. F., & Wilkinson, G. R. (1984). The Raman spectra of ice (I h, II, III, V, VI and IX) as functions of pressure and temperature. *Journal of Physics C: Solid State Physics*, *17*(32), 5833. https://doi.org/10.1088/0022-3719/17/32/017

Mitri, G., Meriggiola, R., Hayes, A., Lefevre, A., Tobie, G., Genova, A., et al. (2014). Shape, topography, gravity anomalies and tidal deformation of Titan. *Icarus*, *236*, 169–177. https://doi.org/10.1016/j.icarus.2014.03.018

Noack, L., Höning, D., Rivoldini, A., Heistracher, C., Zimov, N., Journaux, B., et al. (2016). Water-rich planets: How habitable is a water layer deeper than on Earth? *Icarus*, *277*, 215–236. https://doi.org/10.1016/j.icarus.2016.05.009

Panning, M. P., Stähler, S. C., Huang, H.-H., Vance, S. D., Kedar, S., Tsai, V. C., et al. (2018). Expected seismicity and the seismic noise environment of Europa. *Journal of Geophysical Research: Planets*, *123*(1), 163–179. https://doi.org/10.1002/2017JE005332

Pappalardo, R. t., Vance, S., Bagenal, F., Bills, B. g., Blaney, D. l., Blankenship, D. D., et al. (2013). Science potential from a Europa Lander. *Astrobiology*, *13*(8), 740–773. https://doi.org/10.1089/ast.2013.1003

Phillips, C. B., & Pappalardo, R. T. (2014). Europa Clipper mission concept: Exploring Jupiter's ocean moon. *Eos, Transactions American Geophysical Union*, *95*(20), 165–167. https://doi.org/10.1002/2014EO200002

Pistorius, C. W. F. T., Rapoport, E., & Clark, J. B. (1968). Phase Diagrams of H2O and D2O at High Pressures. *The Journal of Chemical Physics*, *48*, 5509. https://doi.org/10.1063/1.1668248

Prescher, C., & Prakapenka, V. B. (2015). DIOPTAS: A program for reduction of two-dimensional X-ray diffraction data and data exploration. *High Pressure Research*, *35*(3), 223–230. https://doi.org/10.1080/08957959.2015.1059835

Ramírez, R., Neuerburg, N., Fernández-Serra, M.-V., & Herrero, C. P. (2012). Quasi-harmonic approximation of thermodynamic properties of ice Ih, II, and III. *The Journal of Chemical Physics*, *137*(4), 044502. https://doi.org/10.1063/1.4737862

Ramirez, R. M., & Levi, A. (2018). The ice cap zone: A unique habitable zone for ocean worlds. *Monthly Notices of the Royal Astronomical Society*, *477*(4), 4627–4640. https://doi.org/10.1093/mnras/sty761

Salzmann, C. G. (2018). Advances in the experimental exploration of water's phase diagram. *ArXiv:1812.04333 [Cond-Mat]*. Retrieved from. http://arxiv.org/abs/1812.04333

Salzmann, C. G., Radaelli, P. G., Mayer, E., & Finney, J. L. (2009). Ice XV: A new thermodynamically stable phase of ice. *Physical Review Letters*, *103*(10), 105701. https://doi.org/10.1103/PhysRevLett.103.105701

Shaw, G. H. (1986). Elastic properties and equation of state of high pressure ice. *The Journal of Chemical Physics*, *84*(10), 5862. https://doi.org/10.1063/1.449897

Shimizu, H., Nabetani, T., Nishiba, T., & Sasaki, S. (1996). High-pressure elastic properties of the VI and VII phase of ice in dense H_2O and D_2O. *Physical Review B*, *53*(10), 6107–6110. https://doi.org/10.1103/PhysRevB.53.6107

Sohl, F., Choukroun, M., Kargel, J., Kimura, J., Pappalardo, R., Vance, S., & Zolotov, M. (2010). Subsurface water oceans on icy satellites: Chemical composition and exchange processes. *Space Science Reviews*, *153*(1-4), 485–510. https://doi.org/10.1007/s11214-010-9646-y

Sotin, C., & Grasset, O. (2007). Mass-radius curve for extrasolar Earth-like planets and ocean planets. *Icarus*, *191*, 337–351. https://doi.org/10.1016/j.icarus.2007.04.006

Sotin, C., & Tobie, G. (2004). Internal structure and dynamics of the large icy satellites. *Comptes Rendus Physique*, *5*, 769–780. https://doi.org/10.1016/j.crhy.2004.08.001

Span, R. (2000). *Multiparameter equations of state: An accurate source of thermodynamic property data*. Berlin: Springer.
Stähler, S. C., Panning, M. P., Hadziioannou, C., Lorenz, R. D., Vance, S., Klingbeil, K., & Kedar, S. (2019). Seismic signal from waves on Titan's seas. *Earth and Planetary Science Letters*, *520*, 250–259. https://doi.org/10.1016/j.epsl.2019.05.043
Stähler, S. C., Panning, M. P., Vance, S. D., Lorenz, R. D., van Driel, M., Nissen-Meyer, T., & Kedar, S. (2018). Seismic wave propagation in icy ocean worlds. *Journal of Geophysical Research: Planets*, *123*(1), 206–232. https://doi.org/10.1002/2017JE005338
Tammann, G. (1900). Ueber die Grenzen des festen Zustandes IV. *Annalen der Physik*, *307*(5), 1–31. https://doi.org/10.1002/andp.19003070502
Tchijov, V. (2004). Heat capacity of high-pressure ice polymorphs. *Journal of Physics and Chemistry of Solids*, *65*(5), 851–854. https://doi.org/10.1016/j.jpcs.2003.08.019
Tulk, C. A., Gagnon, R. E., Kiefte, H., & Clouter, M. J. (1997). The pressure dependence of the elastic constants of ice III and ice VI. *The Journal of Chemical Physics*, *107*(24), 10,684–10,690. https://doi.org/10.1063/1.474185
Tulk, C. A., Kiefte, H., Clouter, M. J., & Gagnon, R. E. (1997). Elastic constants of ice III, V, and VI by Brillouin spectroscopy. *The Journal of Physical Chemistry B*, *101*(32), 6154–6157. https://doi.org/10.1021/jp963183d
Unterborn, C. T., Desch, S. J., Hinkel, N. R., & Lorenzo, A. (2018). Inward migration of the TRAPPIST-1 planets as inferred from their water-rich compositions. *Nature Astronomy*, *2*(4), 297–302. https://doi.org/10.1038/s41550-018-0411-6
Vance, S., Bouffard, M., Choukroun, M., & Sotin, C. (2014). Ganymede's internal structure including thermodynamics of magnesium sulfate oceans in contact with ice. *Planetary and Space Science*, *96*, 62–70. https://doi.org/10.1016/j.pss.2014.03.011
Vance, S., & Brown, J. M. (2013). Thermodynamic properties of aqueous MgSO4 to 800 MPa at temperatures from −20 to 100 °C and concentrations to 2.5 mol kg^{-1} from sound speeds, with applications to icy world oceans. *Geochimica et Cosmochimica Acta*, *110*, 176–189. https://doi.org/10.1016/j.gca.2013.01.040
Vance, S. D., Kedar, S., Panning, M. P., Stähler, S. C., Bills, B. G., Lorenz, R. D., et al. (2018). Vital signs: Seismology of icy ocean worlds. *Astrobiology*, *18*(1), 37–53. https://doi.org/10.1089/ast.2016.1612
Vance, S. D., Panning, M. P., Stähler, S., Cammarano, F., Bills, B. G., Tobie, G., et al. (2018). Geophysical investigations of habitability in ice-covered ocean worlds: GEOPHYSICAL HABITABILITY. *Journal of Geophysical Research: Planets*, *123*(1), 180–205. https://doi.org/10.1002/2017JE005341
Wagner, W., & Pruß, A. (2002). The IAPWS formulation 1995 for the thermodynamic properties of ordinary water substance for general and scientific use. *Journal of Physical and Chemical Reference Data*, *31*, 387–535.
Wagner, W., Riethmann, T., Feistel, R., & Harvey, A. H. (2011). New equations for the sublimation pressure and melting pressure of H_2O ice Ih. *Journal of Physical and Chemical Reference Data*, *40*(4), 043103. https://doi.org/10.1063/1.3657937
Yen, F., & Chi, Z. (2015). Proton ordering dynamics of H_2O ice. *Physical Chemistry Chemical Physics*, *17*(19), 12,458–12,461. https://doi.org/10.1039/C5CP01529D